

A New Mathematical Approach to the Turbulence Closure Problem

Mohammed A. Azim

Department of Mechanical Engineering, Bangladesh University of Engineering and Technology, Dhaka, Bangladesh

Abstract This study introduces a new mathematical approach (NMA) stating that the remaining small terms upon dominant balance, if retains the essential physics of the original equation, may exist as an additional equation. Application of this additional equation appears to reduce the unclosed governing equations for the two-dimensional turbulent flow to closed ones. The closed form equations due to NMA for the turbulent boundary layer and round jet are solved using a Fully Implicit Numerical Scheme and the Tridiagonal Matrix Algorithm. An overall agreement of the obtained results with the existing database for both types of flow show the capability of NMA in solving the complete closure problem of turbulence.

Keywords Maximal balance, Minimal set, Additional equation, Scaling, Axial slope effect

1. Introduction

The new mathematical approach (NMA) seems to have a common origin with the method of dominant balance which is known to deal with the process of simplification of the equations with small parameters for their solutions. Basically, this simplification considers two or more terms in the equation as large which dominate the solution, other terms being small. The method of dominant balance was introduced by Isaac Newton [1] in 1670-1673 in obtaining approximate solutions of the algebraic equations with small parameters and in considering infinitesimal displacements for the development of differential calculus, and was subsequently developed by Kruskal [2]. Bender and Orszag [3] focused on the simplification methods based on self-consistency and dominant balance for differential equations. Fishaleck and White [4] used Kruskal-Newton diagram for the simplification of a differential equation involving a small parameter and for discovering all possible combinations of maximal balance of the equation. The new mathematical approach states that the remaining negligible terms upon maximal balance of an equation may represent an additional equation. This additional equation may be useful in solving problems with more unknowns than the number of equations.

The study of fluid turbulence by decomposing the flow variables into mean and fluctuating components encounters a situation with more unknowns than the number of equations, called the closure problem. This turbulence closure is a

long-standing unsolved problem of classical physics since the time of Osborne Reynolds [5]. The unclosed differential equations governing the turbulent mean flow are called Reynolds Averaged Navier-Stokes (RANS) equations. As no mathematical method exists, approximations called closure models are used to obtain closed form RANS equations. The closure models are either systematic approximations or intuition and analogy where the latter, in general, is more successful. However, engineering closure models are systematic approximations in combination with intuition and analogy [6]. These engineering closure models have a quite considerable history starting from the first mixing length model [7] to the first k - ϵ model [8] and afterwards various k - ϵ type models. Boussinesq's [9] eddy viscosity concept is the core of these closure models but he did not attempt to solve the RANS equations in any kind of systematic manner.

Similar to engineering closure models, this paper claims the success of systematic approximations in combination with NMA in solving the closure problem. Using the additional equation along with the systematic approximations due to the order of magnitude reasoning, a closed set of equations for the turbulent boundary layer flow as well as for the round jet flow is obtained from their respective unclosed set. The closed sets of equations and the equations for the remaining unclosed terms are solved numerically to discern different characteristics of the flows and thereby to seek the validity of NMA.

2. The New Mathematical Approach

It is often possible to find two or more terms in an equation which dominate the solution, other terms giving only small corrections to the value obtained by neglecting them entirely. In neglecting the small terms, one must

* Corresponding author:

azim@me.buet.ac.bd (Mohammed A. Azim)

Published online at <http://journal.sapub.org/ajfd>

Copyright © 2016 Scientific & Academic Publishing. All Rights Reserved

respect the Kruskal's principle of maximal balance which states that no term should be neglected without a good reason [2]. In maximal balance, the comparable terms constitute a maximal set and the remaining small terms belong to a negligible set. The NMA described herein goes further and states that *the negligible set, if it retains the essential physics of the original equation, may be called a minimal set which acts like an additional equation*. Thus NMA may provide additional equations to get the closed system of equations from the unclosed one.

2.1. Algebraic Basis of NMA

The mathematical justification for NMA is sought through an algebraic equation

$$\psi(x, y) + a(x, y) = \phi(x, y) + b(x, y) \quad (1)$$

where ψ and ϕ are of comparable magnitudes, $\psi \gg a$ and $\phi \gg b$. This equation can be written to a good approximation into two equations as

$$\psi(x, y) = \phi(x, y) \quad (2)$$

$$a(x, y) = S b(x, y) \quad (3)$$

where the scaling parameter S in general is $S(x, y)$ or a constant for identical shapes of a and b . Hence, Eq. (2) may represent the maximal set and Eq. (3) the minimal set.

3. Applications of NMA

NMA is applied to the unclosed governing equations for the two-dimensional (2D) turbulent boundary layer and round jet flows shown in Figs. 1 and 2. Boundary layers are wall shear flows where the fluid viscosity, no matter how small, enforces the no-slip condition at the solid wall. This viscous constraint gives rise to viscosity dominated characteristic velocity and length near the wall while turbulence dominated ones are found away from the wall. On the other hand, jets are free shear flows where fluid coming out from circular orifice mixes with the surrounding fluid and develops through three successive distinct regions, namely initial, intermediate and developed regions. Initial region is characterized by the presence of a potential core that is in laminar state, intermediate region by the transition state and developed (self-similar) region by the fully turbulent state. This jet grows non-linearly in the developing (initial and intermediate) regions and linearly in the developed region. The unclosed governing equations, additional equations due to NMA, primary closed form equations, secondary closed form equations, and their initial and boundary conditions are presented in this section.

3.1. Unclosed Governing Equations

Continuity and RANS equations governing the 2D axisymmetric turbulent flow $(\bar{v}, \theta, \bar{u})$ for a constant property fluid in cylindrical co-ordinates (r, θ, x) are

$$\frac{1}{r} \frac{\partial}{\partial r} (r \bar{v}) + \frac{\partial \bar{u}}{\partial x} = 0 \quad (4)$$

$$\begin{aligned} \bar{v} \frac{\partial \bar{v}}{\partial r} + \bar{u} \frac{\partial \bar{v}}{\partial x} = & -\frac{1}{\rho} \frac{\partial \bar{p}}{\partial r} - \left[\frac{1}{r} \frac{\partial}{\partial r} (r \bar{v}'^2) + \right. \\ & \left. \frac{\partial}{\partial x} (\bar{u}' \bar{v}') - \frac{\bar{w}'^2}{r} \right] + \nu \nabla^2 \bar{v} - \bar{v} \frac{\bar{v}}{r^2} \end{aligned} \quad (5)$$

$$\begin{aligned} \bar{v} \frac{\partial \bar{u}}{\partial r} + \bar{u} \frac{\partial \bar{u}}{\partial x} = & -\frac{1}{\rho} \frac{\partial \bar{p}}{\partial x} - \left[\frac{1}{r} \frac{\partial}{\partial r} (r \bar{u}' \bar{v}') + \frac{\partial}{\partial x} (\bar{u}'^2) \right] \\ & + \nu \nabla^2 \bar{u} \end{aligned} \quad (6)$$

where \bar{v} and \bar{u} are the mean and fluctuating velocity components, similar are other quantities, $\bar{v}' \bar{w}'$ and $\bar{u}' \bar{w}'$ are zero by the circumferential symmetry, ν is the fluid viscosity. The above continuity and RANS equations represent the governing equations for 2D plane turbulent flow $(\bar{u}, \bar{v}, 0)$ in Cartesian co-ordinates (x, y, z) upon substitution of the free $r = 1$, $\partial r = \partial y$, $\bar{w}' \bar{w}' / r = 0$ and $\bar{v} \bar{v} / r^2 = 0$ in them. The system of Eqs. (4)-(6) is not closed because there are more unknowns than the number of equations. In the next section, this unclosed set of equations is made closed by using the additional equation.

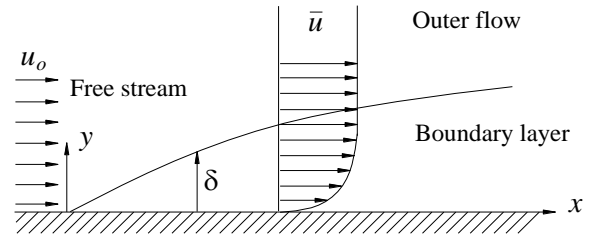


Figure 1. Schematic of a plane boundary layer flow

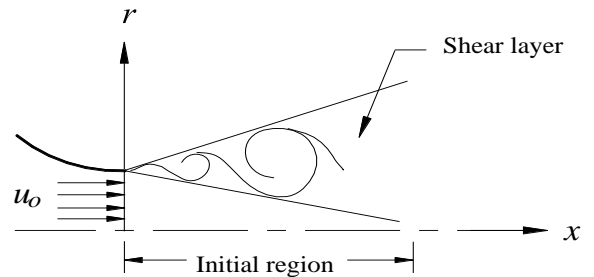


Figure 2. Schematic of a round free jet

3.2. Additional Equation due to NMA

Dimensional analysis provides a great deal of

understanding of the physics involved in the governing equations of a phenomenon that is indispensable in determining both the maximal and minimal sets of the equations. In view of this, dimensional analysis of the RANS equations is carried out by considering the characteristic mean velocity U , velocity fluctuation u , flow width δ and flow length L as the scales of mean and turbulence velocities, diffusion and convection lengths, respectively, with the assumptions [10] that u is comparable to U and δ is comparable to L . Using these velocity and length scales, the orders of magnitude of the terms of Eq. (5) are estimated as follows:

$$\frac{1}{v} \frac{\partial \bar{v}}{\partial r} = O(U^2 \delta / L^2), \quad \frac{1}{u} \frac{\partial \bar{v}}{\partial x} = O(U^2 \delta / L^2),$$

$$\frac{1}{\rho} \frac{\partial \bar{p}}{\partial r} = \frac{w'^2}{r} = \frac{1}{r} \frac{\partial}{\partial r} \left(r \bar{v'^2} \right) = O(u^2 / \delta),$$

$$\frac{\partial}{\partial x} (\overline{u'v'}) = O(u^2 / L), \quad \nu \frac{\partial^2 \bar{v}}{\partial x^2} = O(\nu U \delta / L^3),$$

$$\nu \frac{\partial^2 \bar{v}}{\partial r^2} = O(\nu U / L \delta).$$

The terms of Eq. (5) are written in the order of their magnitudes as

$$\begin{aligned} \frac{1}{\rho} \frac{\partial \bar{p}}{\partial r} + \frac{1}{r} \frac{\partial}{\partial r} \left(r \bar{v'^2} \right) - \frac{w'^2}{r} + \frac{\partial}{\partial x} (\overline{u'v'}) + \frac{1}{v} \frac{\partial \bar{v}}{\partial r} + \\ \frac{1}{u} \frac{\partial \bar{v}}{\partial x} - \nu \nabla^2 \bar{v} + \nu \frac{\bar{v}}{r^2} = 0 \end{aligned} \quad (7)$$

where the first three terms are large and the last five terms are small. This equation represents a balance among the inertia force, pressure force (including normal forces), turbulent shear and viscous forces. The first three terms constitute the traditional maximal set which represents a balance between the pressure force and turbulent normal forces. The last five terms constitute the minimal set which represents a balance among the inertia force, turbulent shear and viscous forces that is the minimal set retains the most essential flow physics of Eq. (7) compared to the traditional maximal set because the former possesses the inertia of fluid motion. Hence, according to NMA, Eq. (7) may be written into two equations as

$$\frac{1}{\rho} \frac{\partial \bar{p}}{\partial r} + \frac{1}{r} \frac{\partial}{\partial r} \left(r \bar{v'^2} \right) - \frac{w'^2}{r} = 0 \quad (8)$$

$$\frac{\partial}{\partial x} (\overline{u'v'}) = -S \left(\frac{1}{v} \frac{\partial \bar{v}}{\partial r} + \frac{1}{u} \frac{\partial \bar{v}}{\partial x} - \nu \nabla^2 \bar{v} + \nu \frac{\bar{v}}{r^2} \right). \quad (9)$$

Equation (9) represents the minimal set and hence provides an additional equation. Comparison of magnitudes

of $\bar{u} \partial \bar{v} / \partial x$ with the left side of this equation provides

$$S = C_I \left(u^2 / U^2 \right) / (\delta / L) \quad (10)$$

where C_I is a constant and $S=S(x)$ since all the flow scales in it are functions of x only.

In boundary layer, the flow scales near the wall due to viscosity dominance become $\bar{u} = O(u)$ and $y = O(\nu / u)$ and other scales remain the same. In case of free jet, only the scales u and δ change through the flow regions, marked by the difference in the flow state [6]. That is in some flow areas some terms are larger than others and relations between the terms vary in different flow areas. The scaling parameter which comprises of an arbitrary constant and some flow scales, accounts the variation of those relations through its transverse and axial dispersions.

3.3. Primary Closed Form Equations

Equation (6) by the order of magnitude reasoning and uniform pressure assumption for thin shear flow ($\delta L < L$) reduces to

$$\frac{1}{v} \frac{\partial \bar{u}}{\partial r} + \frac{1}{u} \frac{\partial \bar{u}}{\partial x} = \frac{1}{r} \frac{\partial}{\partial r} \left(r \nu \frac{\partial \bar{u}}{\partial r} \right) + \frac{1}{r} \frac{\partial}{\partial r} (-r \overline{u'v'}). \quad (11)$$

Hence continuity equation (4), additional equation (9) and momentum equation (11) form a closed system of equations.

3.4. Secondary Closed Form Equations

Comparison of unclosed equations in Sect. 3.1 with closed equations in Sect. 3.3 shows that \bar{p} , $\overline{u'u'}$, $\overline{v'v'}$ and $\overline{w'w'}$ are left unknown. With a view to obtain the equations for the unknown terms, Eq. (5) may be written as

$$\begin{aligned} \frac{1}{v} \frac{\partial \bar{v}}{\partial r} + \frac{1}{u} \frac{\partial \bar{v}}{\partial x} = -\frac{1}{\rho} \frac{\partial \bar{p}}{\partial r} - \left[\frac{\partial}{\partial r} \left(r \bar{v'^2} \right) + \frac{\partial}{\partial x} (\overline{u'v'}) \right] \\ + \nu \nabla^2 \bar{v} - \nu \frac{\bar{v}}{r^2} \end{aligned} \quad (12)$$

being $\overline{v'v'}$ and $\overline{w'w'}$ are equal in axisymmetric flow and $\overline{v'v'}$ can be solved from this equation for the known \bar{p} .

Afterwards $\overline{w'w'}$ can be calculated from Eq. (5) because all other quantities are already known.

Neglecting the small viscous term, Eq. (6) may be read as follows

$$\frac{1}{v} \frac{\partial \bar{u}}{\partial r} + \frac{1}{u} \frac{\partial \bar{u}}{\partial x} - \frac{1}{r} \frac{\partial \tau}{\partial r} = -\frac{1}{\rho} \frac{\partial \bar{p}}{\partial x} - \frac{\partial}{\partial x} (\overline{u'^2}) \quad (13)$$

where $\tau = \nu \partial \bar{u} / \partial r - \overline{u'v'}$ is the effective shear stress. In order to solve the mean static pressure \bar{p} , Eq. (13) may be written by neglecting the small normal stress term as

$$-\frac{\partial \bar{u}}{\partial r} + u \frac{\partial \bar{u}}{\partial x} - \frac{1}{r} \frac{\partial \bar{\tau}}{\partial r} = -\frac{1}{\rho} \frac{\partial \bar{p}}{\partial x} \quad (14)$$

where by the order of magnitude arguments, left side is a maximal set and right side a minimal set of single small element. This singleton is trivial, as a result, the minimal set is obtained by including a small fraction of the left side into the trivial set, as an extension of NMA, which may be called an extended NMA. Equation (14) is written in the form of Eq. (1) as

$$(1-S) \left(-\frac{\partial \bar{u}}{\partial r} + u \frac{\partial \bar{u}}{\partial x} \right) + S \left(-\frac{\partial \bar{u}}{\partial r} + u \frac{\partial \bar{u}}{\partial x} - \frac{1}{r} \frac{\partial \bar{\tau}}{\partial r} \right) = (1-S) \left(\frac{\partial \bar{\tau}}{\partial r} \right) - \frac{1}{\rho} \frac{\partial \bar{p}}{\partial x} \quad (15)$$

where S is a small scaling parameter. Now following NMA, the minimal set may be extracted as

$$S \left(-\frac{\partial \bar{u}}{\partial r} + u \frac{\partial \bar{u}}{\partial x} - \frac{1}{r} \frac{\partial \bar{\tau}}{\partial r} \right) = -\frac{1}{\rho} \frac{\partial \bar{p}}{\partial x}. \quad (16)$$

Equation (14) represents a balance among the forces due to inertia, effective shear and pressure. The above minimal set also represents a balance among the same forces implying that the minimal set retains all the essential flow physics of Eq. (14). Hence equation for solving \bar{p} is

$$\frac{1}{\rho} \frac{\partial \bar{p}}{\partial x} = -S \left(-\frac{\partial \bar{u}}{\partial r} + u \frac{\partial \bar{u}}{\partial x} - \frac{1}{r} \frac{\partial \bar{\tau}}{\partial r} \right). \quad (17)$$

Equation for solving the axial normal stress $\bar{u}'u'$ may be obtained from Eq. (13) as

$$\frac{\partial}{\partial x} (\bar{u}'^2) = -S \left(\frac{1}{\rho} \frac{\partial \bar{p}}{\partial x} + \frac{\partial \bar{u}}{\partial r} + u \frac{\partial \bar{u}}{\partial x} - \frac{1}{r} \frac{\partial \bar{\tau}}{\partial r} \right). \quad (18)$$

Radial normal stress $\bar{v}'v'$ can be solved by scaling Eq. (12) in the form

$$\frac{\partial}{\partial r} (\bar{v}'^2) = -S \left[\frac{1}{\rho} \frac{\partial \bar{p}}{\partial r} + \frac{\partial \bar{v}}{\partial r} + u \frac{\partial \bar{v}}{\partial x} + \frac{\partial}{\partial x} (\bar{u}'v') - \nu \nabla^2 \bar{v} + \nu \frac{\partial \bar{v}}{\partial r^2} \right] \quad (19)$$

and the azimuthal normal stress $\bar{w}'w'$ can be solved by scaling Eq. (5) as

$$\frac{\bar{w}'^2}{r} = S \left[\frac{\partial \bar{v}}{\partial r} + u \frac{\partial \bar{v}}{\partial x} + \frac{1}{\rho} \frac{\partial \bar{p}}{\partial r} + \frac{1}{r} \frac{\partial}{\partial r} (r \bar{v}'^2) + \frac{\partial}{\partial x} (\bar{u}'v') - \nu \nabla^2 \bar{v} + \nu \frac{\partial \bar{v}}{\partial r^2} \right]. \quad (20)$$

Stress $\bar{w}'w'$ does not appear in the RANS equations for plane boundary layer flow to add to the closure problem. So it can be obtained from the turbulent stress tensor

$$-\bar{u}'_i u'_j = \frac{1}{3} \delta_{ij} (-\bar{u}'_k u'_k) + \nu_t \left(\frac{\partial \bar{u}_i}{\partial x_j} + \frac{\partial \bar{u}_j}{\partial x_i} \right) \quad (21)$$

which is in analogy to the constitutive equation for laminar flow for $-\bar{u}'_i u'_j = \tau_{ij}^t / \rho$ and $-\bar{u}'_k u'_k = \nu_t \partial \bar{u}_k / \partial x_k$, and in 2D flow for $i=j=3$ reduces to

$$\bar{w}'^2 = (\bar{u}'^2 + \bar{v}'^2) / 2, \quad (22)$$

validity of which is discussed later.

3.5. Initial and Boundary Conditions

In boundary layer flow, the initial conditions are $\bar{u}(0, y) = u_o$, $\bar{p}(0, y) = p_o$ and $\phi(0, y) = 0$ where u_o and p_o are the uniform free-stream velocity and pressure, and ϕ is the general flow variable. The boundary conditions are ϕ attains free-stream values at the boundary layer edge, $\partial \phi / \partial x = 0$ at the outflow and $\phi = 0$ at the wall.

In free jet flow, the initial conditions are $\bar{u}(r \leq r_o, 0) = u_o$, $\bar{u}(r > r_o, 0) = 0$, $\bar{v}(r, 0) = 0$, $\bar{u}'^2(r \leq r_o, 0) = 0.004 u_o^2$ and $\bar{p}(r \leq r_o, 0) = 0.002 \rho u_o^2$ where r_o and u_o are the radius and uniform velocity at the jet exit. The boundary conditions are ϕ attains ambient conditions at the jet outer edge, $\partial \phi / \partial x = 0$ at the outflow and $\partial \phi / \partial r = 0$ at the axis of symmetry except $\bar{v} = 0$.

4. Numerical Methods

It is already mentioned that eddy viscosity concept is the core of all turbulence closure models. As a result, hardly there is any standard numerical scheme for solving the closed form Eqs. (4), (9) and (11). This necessitates to writing the momentum equation (11) in the form

$$\frac{\partial \bar{u}}{\partial r} + u \frac{\partial \bar{u}}{\partial x} = \frac{1}{r} \frac{\partial}{\partial r} \left(\nu r N \frac{\partial \bar{u}}{\partial r} \right) \quad (23)$$

using $-\bar{u}'v' = \nu_t (\partial \bar{u} / \partial r)$ and $N = (\nu + \nu_t) / \nu$, and also necessitates to writing Eq. (9) as

$$\nu_t = \left(\frac{\partial \bar{u}}{\partial r} \right)^{-1} \int_0^x S \left(\frac{\partial \bar{v}}{\partial r} + u \frac{\partial \bar{v}}{\partial x} - \nu \nabla^2 \bar{v} + \nu \frac{\partial \bar{v}}{\partial r^2} \right) dx \quad (24)$$

where ν_t is the eddy viscosity and N is the normalized effective viscosity.

Further N is written in a recurrence relation, using the trapezoidal integration formula with the first degree polynomial and Eq. (24) in $N = (\nu + \nu_t)/\nu$, in the form

$$N_{i,j} = 1 + \left[\left(N_{i-1,j-1} \right) \left(\nu \frac{\partial \bar{u}}{\partial r} \right)_{i-1,j^+} + 0.5 \Delta x_m \left(f_{i-1,j} f_{i,j} \right) \left(\nu \frac{\partial \bar{u}}{\partial r} \right)_{i,j}^{-1} \right] \quad (25)$$

where $\Delta x_m = (x_i - x_{i-1})$ and

$$f_{i,j} = S \left(\bar{v} \frac{\partial \bar{v}}{\partial r} + \bar{u} \frac{\partial \bar{v}}{\partial x} - \nu \nabla^2 \bar{v} + \nu \frac{\partial \bar{v}}{\partial r} \right)_{i,j} \quad (26)$$

The closed set of Eqs. (4), (23) and (25) are solved numerically using the Fully Implicit Numerical Scheme (FINS) [11] and Tridiagonal Matrix Algorithm (TDMA) [12] for the solutions of \bar{u} , \bar{v} and $\bar{u}'\bar{v}'$. There second-order upwind interpolation is used for convective coefficients of Eq. (23). The solutions of \bar{p} , $\bar{u}'\bar{u}'$, $\bar{v}'\bar{v}'$ and $\bar{w}'\bar{w}'$ are obtained from Eqs. (17)-(20) by writing them in finite difference form except Eq. (19) in the integral form for the solution of $\bar{v}'\bar{v}'$. In boundary layer flow, the solution of $\bar{w}'\bar{w}'$ is obtained by using Eq. (22).

4.1. Grid Specifications

Schematic of the computational domains for the boundary layer is $L_x=0.4m$ and $L_y=0.6m$ in x - and y -directions as seen in Fig. 1 and for the jet flow $L_r=10d$ and $L_x=30d$ in r and x -directions where $d=0.04m$ is the jet diameter at the exit as in Fig. 2. Grid spacing is uniform in x - and variable in y -directions such that $\Delta y_{j+1} = K \Delta y_j$ and $\Delta y_1 = L_y(K-1)/(K^{n_j}-1)$ where $K=1.12$ for the boundary layer and $K=1.02$ for the jet flow. Here all the flow properties are located at the same grid point as the pressure gradient is absent in the set of primary closed form equations to be solved. The under-relaxation factors used for \bar{u} , \bar{v} and N are equal to 0.7 for each. The used numerical scheme is second order accurate and found to provide converged solution in 19 iterations which is accurate to six decimal places for the mean velocity \bar{u}/u_o . To avoid the necessity of special grid specifications near the wall to account the steep variation of flow properties, certain variation of $\nu_t = \kappa u_* y$ is assumed within $y/\delta < 0.05$ in accordance with Townsend [13] and Klebanoff [14] data, instead of ν_t in Eq. (24), where $\kappa=0.4$ is the von Karman constant and u_* is the friction velocity.

4.2. Grid Convergence Test

Grid convergence test is carried out with the three different grid sizes termed as coarse, medium and fine for

$n_i \times n_j$ equal to 431×61 , 461×66 and 501×71 where n_i and n_j are the number of grid points in x and y -directions for the boundary layer flow, and 1021×121 , 1111×134 and 1201×145 in x and r -directions for the jet flow. Figure 3 shows the transverse profiles \bar{u}/u_o of the boundary layer at $x/L=0.5$ for the three different grid resolutions with $Re=8 \times 10^5$ where $Re=u_o L/\nu$ is the Reynolds number. Figure 4 exhibits the radial profiles \bar{u}/u_o of the round jet with $Re=3 \times 10^4$ at the location of $x/d=3$ for the three different grid resolutions where $Re=u_o d/\nu$. Grid refinement shows successful convergence with the three grid sizes. The results presented in this paper are obtained by using the fine mesh.

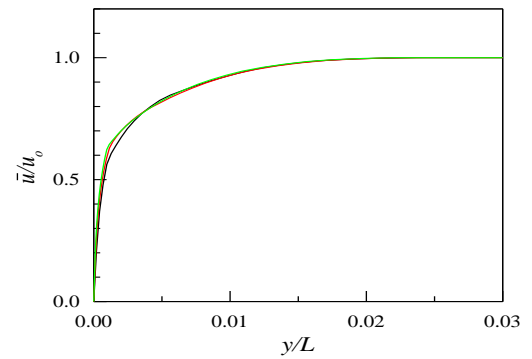


Figure 3. Mean velocity profiles at $x/L=0.5$. Grid points $n_i \times n_j$: 431x61 (—), 461x66 (—), 501x71 (—)

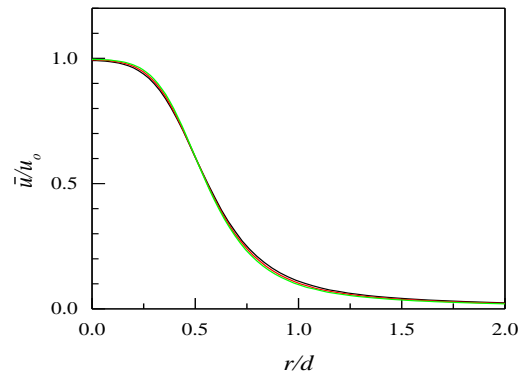


Figure 4. Mean velocity profiles at $x/d=3$. Grid points $n_i \times n_j$: 1021x121 (—), 1111x134 (—), 1201x145 (—)

5. Results and Discussion

The unclosed set of equations governing the turbulent flow, continuity and RANS, is made closed using the additional equations due to NMA. The closed set of Eqs. (4), (23) and (25) is solved both for the boundary layer and free jet flows for the given initial and boundary conditions using FINS and TDMA. Details of the scale factor S for calculating $\bar{u}'\bar{v}'$, \bar{p} , $\bar{u}'\bar{u}'$, $\bar{v}'\bar{v}'$ and $\bar{w}'\bar{w}'$ from Eq. (9) and Eqs.

(17)-(20), respectively, are described in the next subsections. The flow development, mean velocity, turbulent shear and normal stresses, and mean static pressure from the present simulation for both types of flow are presented in this section, and compared with the experimental data of Klebanoff [14] for $R_\theta=7500$, Murlis *et al.* [15] for $R_\theta=5000$, Coles [16] for $R_\theta=5000$ and McQuaid [17] with little air injection $v_w/u_o \approx 0.003$ for $R_\theta=5000$ for the boundary layer flow, and compared with the experimental data of Fellouah *et al.* [18] for $R_e=3 \times 10^4$, Fellouah and Pollard [19] for $R_e=3 \times 10^4$ and Hussein *et al.* [20] in the self-similar region ($x/d \geq 30$) for $R_e=9.6 \times 10^4$ for the jet flow.

5.1. Boundary Layer Flow

Simulation is made for the turbulent boundary layer due to air flow over the flat plate with zero pressure gradient at $R_\theta=2170$ ($R_e=8 \times 10^5$) where $R_\theta=u_o \theta/\nu$ is the Reynolds number and θ is the momentum thickness. The shapes of u^2/U^2 and δ/L are identical [21] to $x^{-0.2}$ that renders Eq. (10) to $S=C_I$. The numerical scheme is found to converge to a stable solution for $C_I=3.2$ which appears in Eq. (25) through $f_{i,j}$.

5.1.1. Flow Development

Development of the boundary layer is shown schematically in Fig. 1 where its thickness δ is located at $\bar{u}/u_o=0.99$. The growths of δ and θ represented by the Reynolds numbers R_δ and R_θ are shown in Fig. 5 against x/L where $R_\delta=u_o \delta/\nu$. There the staircase boundary layer edge obtained from the present simulation is shown by the best fit. It seems from the figure that boundary layer thickness is one order higher than momentum thickness which is consistent with the theoretical results [21].

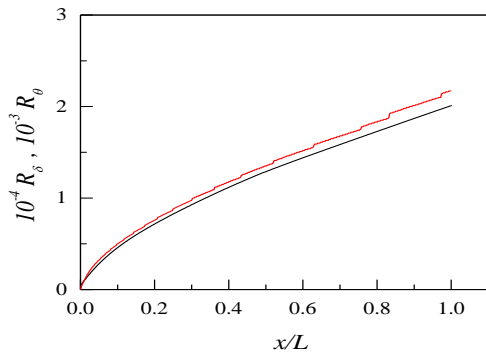


Figure 5. Streamwise growth of the boundary layer. R_δ (—), R_θ (—)

Figure 6(a) shows the streamwise variation of the friction coefficient $C_f = 2\tau_w/\rho u_o^2$ against R_θ where $\tau_w = \rho u_*^2$ is the wall shear stress. Muralis *et al.* [15] data of friction coefficient added in the figure for comparison are seen in acceptable agreement with that of the present simulation.

Figure 6(b) shows the streamwise variation of the shape factor H against R_θ where H is the ratio of displacement thickness to momentum thickness with their usual definitions. The value of H in the figure indicates a turbulent flow although the Reynolds number is low. Comparison shows that Coles [16] data are in good agreement with that of the present simulation.

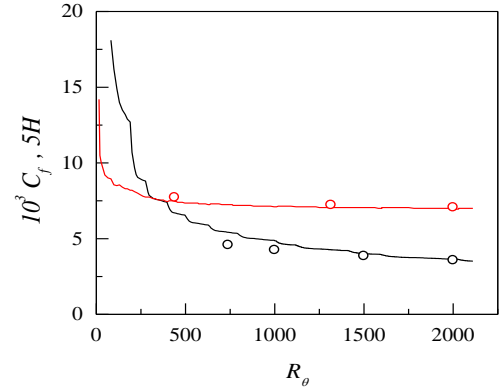


Figure 6. Streamwise variation of (a) friction coefficient: present (—), Muralis *et al.* data [15] (o), (b) shape factor: present (—), Coles data [16] (o)

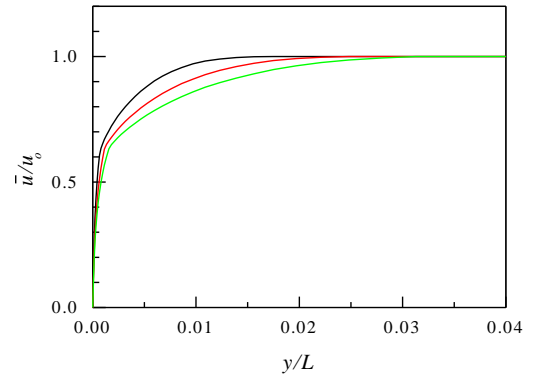


Figure 7. Mean streamwise velocity profiles at x/L : 0.3 (—), 0.5 (—), 1.0 (—)

Mean streamwise velocity \bar{u}/u_o for the boundary layer is plotted in Fig. 7 against the transverse distance y/L at the streamwise locations $x/L=0.3, 0.6$ and 1.0 . As the streamwise distance increases, the boundary layer grows and velocity within it decreases due to increasing loss of momentum at the wall. Dimensionless mean velocity $u^+ = \bar{u}/u_*$ is shown against $y^+ = u_* y/\nu$ in Fig. 8 at three different locations $x/L=0.3, 0.6$ and 1.0 . Mean velocity profiles follow the log-law $u^+ = \ln(y^+)/\kappa + A$, with constants $\kappa=0.4$ and $A=5$ which are close to their widely known values. The velocity profiles have the logarithmic region between $y^+ \approx 30$ and $y^+ \approx 260$ where the upper limit depends on the Reynolds number of the flow.

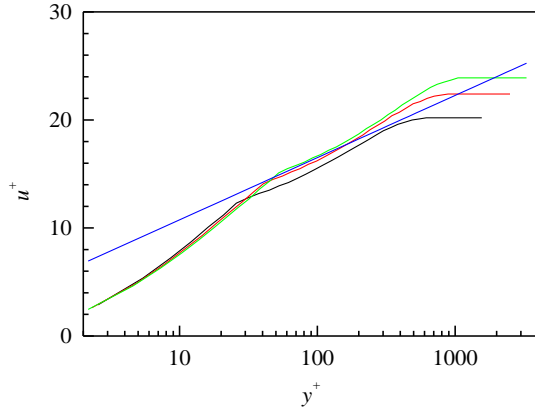


Figure 8. Mean velocity profiles in semi-log axes. Lines as in Fig. 7. Log-law (—)

5.1.2. Flow Properties

Mean streamwise velocity \bar{u} is plotted in similarity co-ordinates in Fig. 9 at $x/L=0.3, 0.6$ and 1.0 using the velocity scale u_o and length scale δ . The scalings are found to collapse the velocity profiles very well. The \bar{u} velocity profile of the present results is compared with Klebanoff [14] data and found to be in good agreement. Mean transverse velocity \bar{v} is plotted in the similarity co-ordinates $(\bar{v}/u_o)/(\delta/L)$ and y/δ in Fig. 10 which shows good collapse of the transverse velocity profiles right from the wall outward. In the figure, these velocity profiles show an outward flow at all x - locations of the boundary layer. It is noteworthy that the plot of \bar{v} -velocity profiles does not collapse in similarity co-ordinates \bar{v}/u_o and y/δ (not shown) which is consistent with the existing literature [22].

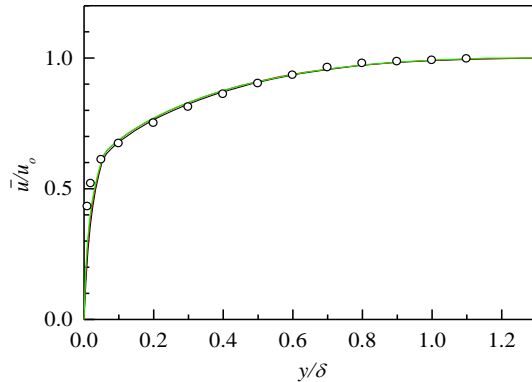


Figure 9. Mean streamwise velocity profiles. Lines as Fig. 7. Klebanoff data [14] (o)

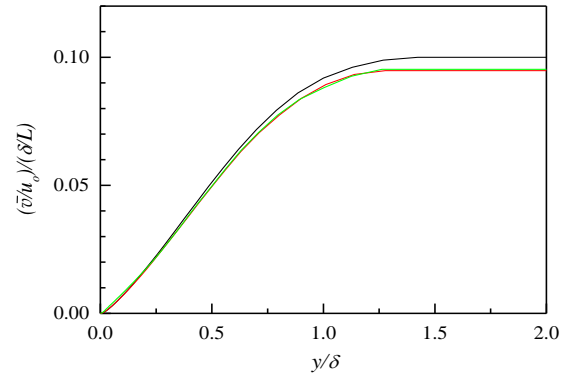


Figure 10. Mean transverse velocity profiles. Lines as Fig. 7

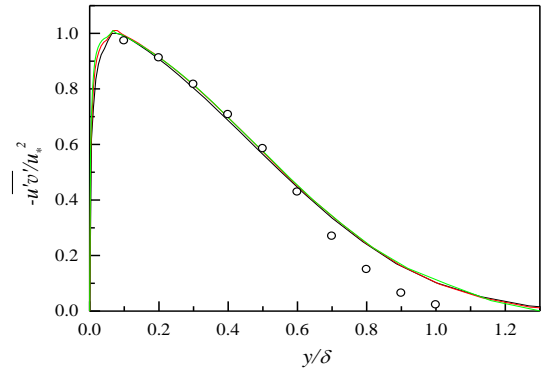


Figure 11. Reynolds shear stress profiles at $x/L: 0.3$ (—), 0.6 (—), 1.0 (—). Klebanoff data [14] (o)

Figure 11 displays the collapse of $\overline{u'v'}$ profiles in similarity co-ordinates $\overline{u'v'}/u_o^2$ and y/δ right from the wall at the positions $x/L=0.3, 0.6$ and 1.0 . This shear stress is calculated using the eddy viscosity formula

$$-\overline{u'v'} = \nu(N - I) \left(\partial \bar{u} / \partial y \right). \quad (27)$$

Comparison shows that Klebanoff [14] data are in good agreement with the present simulation. Again, the shear stress is calculated by integrating Eq. (9) along with the continuity equation as

$$-\overline{u'v'} = \overline{u} \overline{v} + \int_0^x \left(\partial \bar{v}^2 / \partial y - \nu \nabla^2 \bar{v} \right) dx \quad (28)$$

where $S=C_I$ not shown in the equation. This shear stress is depicted in Fig. 12 against y/δ . It is apparent that calculated shear stress with $S=3.2$ is in excellent agreement with Klebanoff [14] data and thus validates Eq. (9) as an additional equation to achieve turbulence closure.

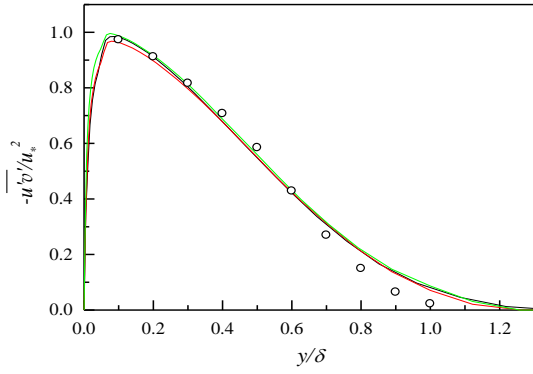


Figure 12. Reynolds shear stress by Eq. (9). Lines and symbol as in Fig. 11

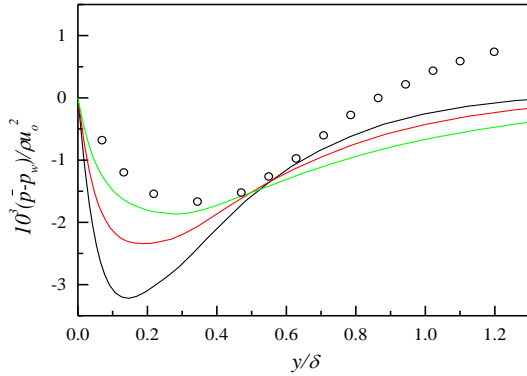


Figure 13. Mean static pressure profiles. Lines as in Fig. 11. McQuaid data [17] (o)

Solution for mean static pressure with reference to the wall static pressure p_w is obtained from Eq. (17). The normalized pressure $\overline{p}/\rho u_o^2$ is plotted in Fig. 13 against y/δ at the streamwise positions $x/L=0.3, 0.6$ and 1.0 . The obtained solution requires $S = 0.04(\delta/L)$ close to the wall and $S = 0.27(\delta/L)$ away from the wall. The profile of $(\overline{p} - p_w)/\rho u_o^2$ at $x/L=1$ ($R_\theta=2170$) is compared with the experimental data [17] at $R_\theta=2060$ and found in qualitative agreement where the disagreement is due to lower p_w in the experiment induced by the fluid injection.

The solutions of $\overline{u'u'}$ and $\overline{v'v'}$ are obtained from Eqs. (18) and (19), respectively, for $S=0.025$ and $S=1.3$. The solution of $\overline{w'w'}$ is obtained using Eq. (22). Figure 14 displays the stresses $\overline{u'u'}$, $\overline{v'v'}$ and $\overline{w'w'}$ as functions of y/δ at $x/L=1$. Klebanoff [14] data for the normal stresses added for comparison exhibit good agreement with that of the present simulation.

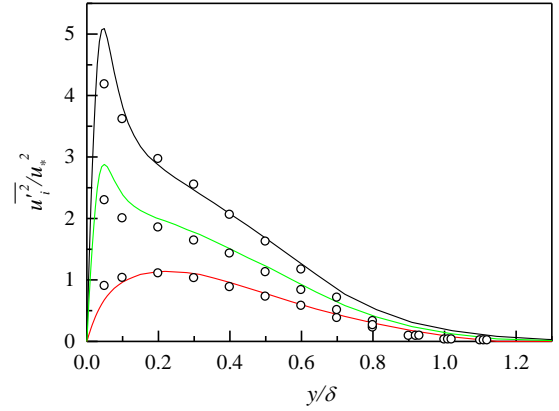


Figure 14. Turbulent stress profiles at $x/L=1$. $\overline{u'u'}/u_*^2$ (—), $\overline{v'v'}/u_*^2$ (—), $\overline{w'w'}/u_*^2$ (—). Klebanoff data [14] (o)

5.1.3. Estimation of Scale Factor

Scale factor S is estimated for calculating $\overline{u'v'}$ from Eq. (9), \overline{p} , $\overline{u'u'}$ and $\overline{v'v'}$ from Eqs. (17)-(19) by comparing the orders of magnitude of the shear stress term with the inertia as $S=C_1$, comparing the pressure with the shear stress as $S=C_2(\delta/L)$, comparing the axial normal stress with the pressure as $S=C_3$ and comparing the transverse normal stress with the pressure as $S=C_4$, respectively, where C_1, C_2, C_3 and C_4 are constants. Equation (17) for \overline{p} possesses parametric scale factor while Eqs. (18) and (19) for $\overline{u'u'}$ and $\overline{v'v'}$ possess constant scale factor. As a result, the solution of \overline{p} requires a small value of C_2 near the wall and a large value away from the wall due to the presence of viscosity dominated flow scales near the wall and turbulence dominated one away from the wall.

5.2. Round Jet Flow

Simulation is made for the round free air jet with 40 mm diameter and top-hat velocity at the exit with $Re=3 \times 10^4$. The numerical scheme is found to converge to produce a stable solution for $S = 0.01(x/d)^{1.5}$ at $x/d \leq 15$ and for $S=1$ at $x/d > 15$ where S appears in Eq. (25) through $f_{i,j}$. Such expressions for S come from the reduction of Eq. (10) at $x/d \leq 15$ due to $u^2/U^2 \sim x$ and $\delta L \sim x^{-0.5}$, and at $x/d > 15$ due to the constant values of both u^2/U^2 and δL .

5.2.1. Flow Development

In the present simulation, initial region terminates at $x/d=5.2$ at which $u_c=0.98u_o$ and intermediate region terminates at $x/d \approx 15$ beyond which the jet grows linearly. The obtained location for the latter region is close to the data of Ferdman *et al.* [23] for $Re=2.4 \times 10^4$ and Xu and Antonia

[24] for $Re=8.6 \times 10^4$. Direct numerical simulation of a round jet performed by Boersma *et al.* [25] for $Re=2.4 \times 10^3$ shows that self-similar state of the Reynolds stress appears at $20 < x/d < 35$, although general consensus [26] is that fully developed region occurs approximately at $x/d \geq 30$. The conditions for self-similarity obtained from axial RANS equation (11) by neglecting the viscous effect dictate $U=U(x)$ or constant [27] but presence of the pressure or normal stress gradient in the equation restricts U to be constant.

Axial decay of the centerline mean velocity u_c is shown in Fig. 15 that follows the inverse relation with downstream distance given by

$$u_o / u_c = (Ad)^{-1} (x - x_o) \quad (29)$$

where A is the mean velocity decay constant. Experimental data [18] added for comparison indicate somewhat higher decay of the mean velocity. Current simulation of the jet is found to yield $A = 6.25$ and $x_o = -0.69d$ which are close to the existing data [23, 28].

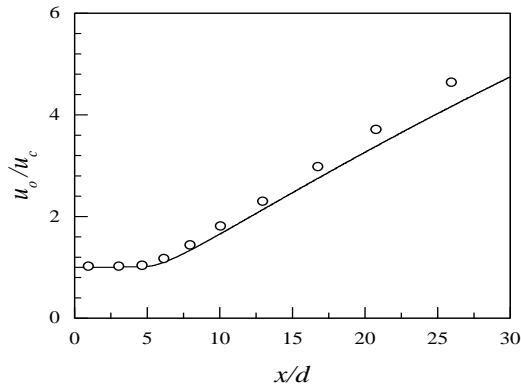


Figure 15. Centerline mean velocity. Present (—), Fellouah *et al.* data [18] (o)

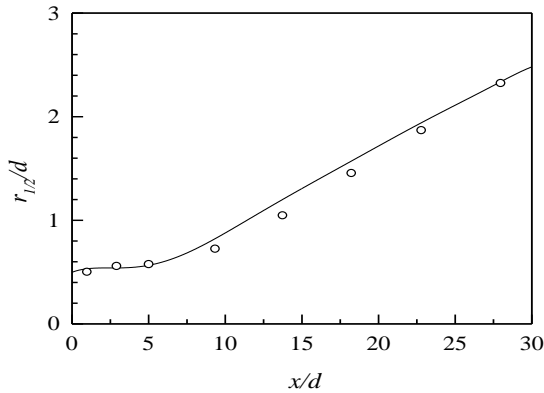


Figure 16. Growth of jet half-width. Present (—), Fellouah and Pollard data [19] (o)

Growth of the jet half-width $r_{1/2}$ is plotted in Fig. 16 where $r_{1/2}$ is the radial distance from the jet axis to which mean velocity is half of the centerline velocity. Present simulation illustrates linear growth of the half-width as

$$r_{1/2} / d = B(x/d) + 0.082 \quad (30)$$

for $B=0.082$ at $x/d > 15$. Fellouah and Pollard data [19] provided for comparison exhibit close agreement with that of the present simulation.

Mean axial velocity \bar{u} / u_o is presented in Fig. 17 against the radial distance r/d at the axial locations $x/d=3, 10$ and 15 . As the axial distance increases, the jet grows due to entrainment of the ambient fluid and its maximum velocity decreases due to the loss of momentum by the interaction with the ambient fluid.

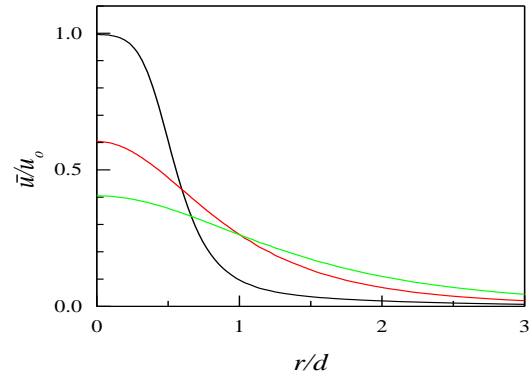


Figure 17. Mean axial velocity profiles at x/d : 3 (—), 10 (—), 15 (—)

5.2.2. Flow Properties

Radial profiles of mean axial velocity \bar{u} / u_o are plotted in Fig. 18 at axial positions $x/d=3, 10$ and 15 . Fellouah *et al.* [18] data added for comparison show reasonable agreement with those of the present simulation. Again, radial profiles of this velocity \bar{u} are displayed in Fig. 19 in similarity co-ordinates \bar{u} / u_c and $r/(x-x_o)$ at $x/d=10, 20$ and 30 , and found in good collapse. Hussein *et al.* [20] data of \bar{u} -velocity are found in acceptable agreement with the present results. Mean radial velocity \bar{v} is plotted in Fig. 20 in similarity axes \bar{v} / u_c and $r/(x-x_o)$ at $x/d=10, 20$ and 30 . The \bar{v} -velocity in Pope [10] from Hussein *et al.* laser doppler anemometer data included for comparison are found in reasonable agreement with that of the present simulation but run off at $r/(x-x_o) > 0.15$ and the velocity becomes negative. This is because of more decay of the jet in Hussein *et al.* ($A^{-1}=0.17$) causes more entrainment of the ambient fluid towards the jet centerline compared to the present simulation ($A^{-1}=0.16$).

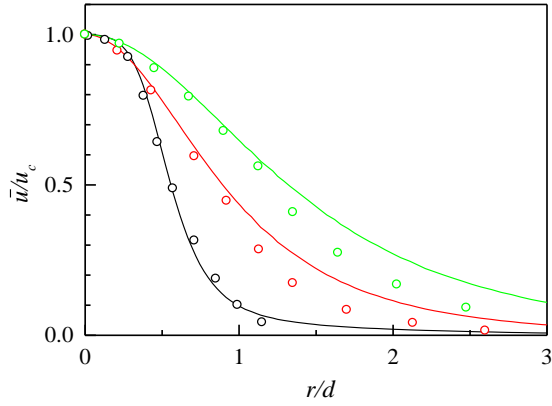


Figure 18. Mean axial velocity profiles. Lines as in Fig. 17. Fellouah *et al.* data [18] (x/d : 3 (o), 10 (o), 15 (o))

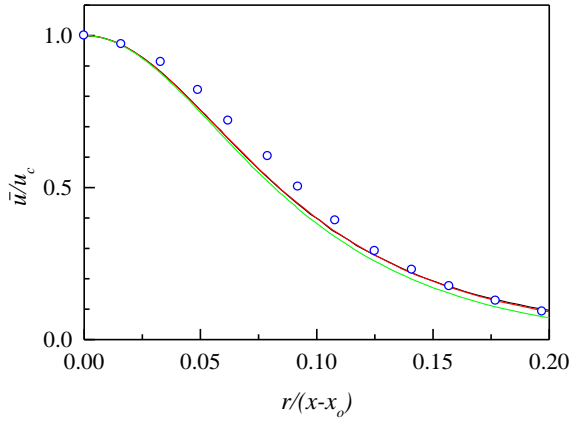


Figure 19. Mean axial velocity profiles at x/d : 10 (—), 20 (—), 30 (—). Hussein *et al.* data [20] (o)

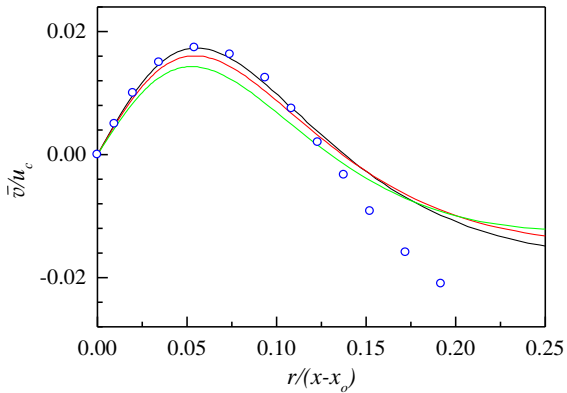


Figure 20. Mean radial velocity profiles. Lines as in Fig. 19. Data from Pope [10] (o)

Reynolds shear stress $\overline{u'v'}/u_c^2$ is depicted in Fig. 21 against r/d at $x/d=3, 10$ and 15 . This shear stress is calculated using eddy formula in Eq. (27). The profiles of $\overline{u'v'}/u_c^2$ are

seen in satisfactory agreement with Fellouah *et al.* [18] data, although the stress level is somewhat different in the simulation. Lower decay of the jet in the present simulation ($A^{-1}=0.16$) than the experiment ($A^{-1}=0.18$) causes lower level of $\overline{u'v'}/u_o^2$ as appears in the figure for $\overline{u'v'}/u_c^2$ at $x/d=3$

but normalization by u_c^2 masks this fact at $x/d=10$ and 15 . This shear stress is plotted again in Fig. 22 against $r/(x-x_o)$ at $x/d=10-30$. Data of Fellouah *et al.* [18] and Hussein *et al.* [20] added for comparison show close agreement with that of the present simulation.

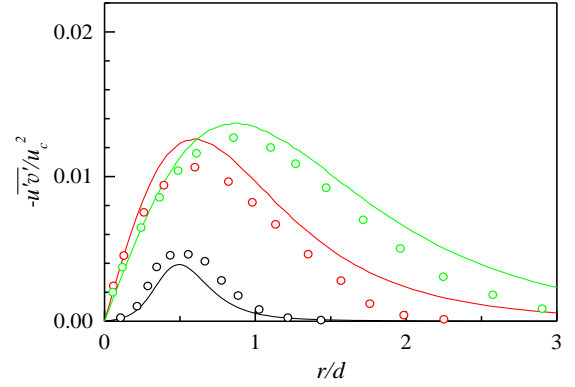


Figure 21. Reynolds shear stress profiles at x/d : 3 (—), 10 (—), 15 (—). Fellouah *et al.* [18] (x/d : 3 (o), 10 (o), 15 (o))

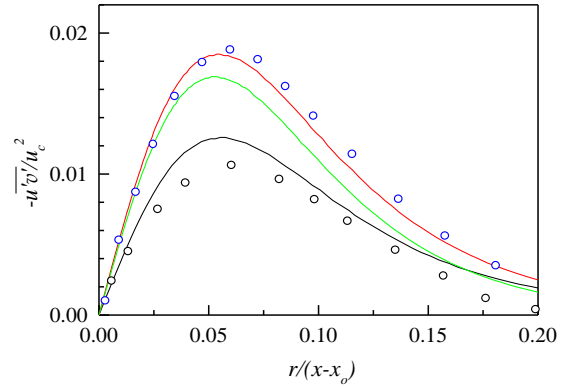


Figure 22. Reynolds shear stress profiles at x/d : 10 (—), 20 (—), 30 (—). Fellouah *et al.* [18] (o), Hussein *et al.* [20] (o)

In order to seek validity for primary closure, $\overline{u'v'}$ is calculated from Eq. (9) for $S=0.043$ in the initial region, $S = 0.0075(x/d)^{1.5}$ in the intermediate region and

$S = 0.02(x/d)^{-1}$ in the developed region where S for different regions are obtained by simple comparison of magnitudes of the appropriate terms as shown in the next section. This calculated shear stress is seen to increase rapidly in the downstream from $x/d=10-30$ as shown in Fig.

23 indicating that S cannot accommodate the axial evolution of turbulent shear stress unlike the boundary layer flow. This is because turbulent stresses gradually increase and then decrease along the jet flow, i.e. their slopes change from positive to negative contrary to the boundary layer flows as observed in experiments and simulations (e.g. [29, 30]).

While $S = -10.6(x/d)^{-1}$ obtained by comparing the magnitudes of the terms as above but with $-S$ instead of $+S$ at $x/d > 15$ (exemplified later) to account such negative slope effect (NSE) proves to be able to predict the evolution of the shear stress as demonstrated in Fig. 24. Fellouah *et al.* [18] and Hussein *et al.* [20] data added for comparison are found in good agreement with the present simulation.

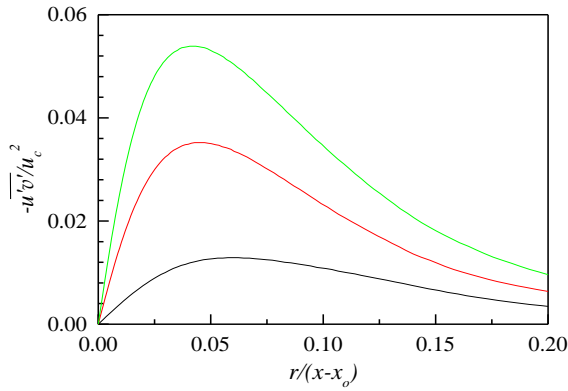


Figure 23. Reynolds shear stress by Eq. (9) without NSE. Lines as in Fig. 22

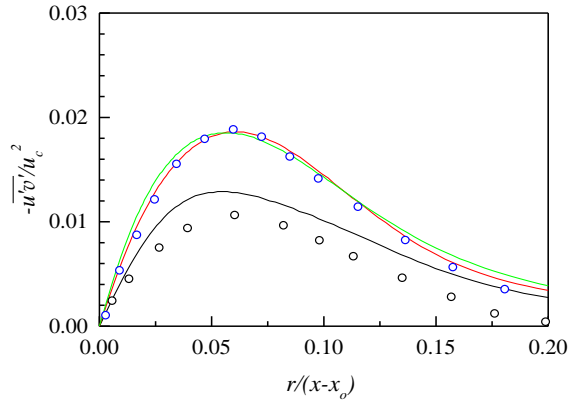


Figure 24. Reynolds shear stress profiles by Eq. (9) with NSE. Lines as in Fig. 22. Data of Fellouah *et al.* [18] ($x/d: 10$ (o)) and Hussein *et al.* [20] (\odot)

Solution for the mean static pressure is obtained from Eq. (17) for positive pressure at the jet exit with reference to the ambient pressure p_o . The normalized pressure $\bar{p}/\rho u_c^2$ is shown in Fig. 25 against r/d at the axial positions $x/d=3, 10$ and 15 . The solutions are obtained for $S = 0.025(x/d)^{-0.5}$

in the initial region, $S = 0.035(x/d)^{-0.5}$ in the intermediate region and $S = -0.2(x/d)^{-1}$ in the developed region. Here S for the developed region of the jet is obtained by taking NSE because pressure also changes slope at some distance downstream along the flow. Figure 26 displays $\bar{p}/\rho u_c^2$ as a function of $r/(x-x_o)$ at $x/d=10-30$ where the centerline pressure is seen to decrease in the downstream as may be observed from Quinn [29] data.

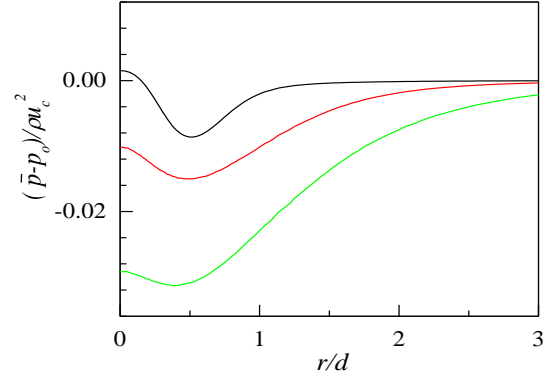


Figure 25. Mean static pressure profiles at $x/d: 3$ (—), 10 (—), 15 (—)

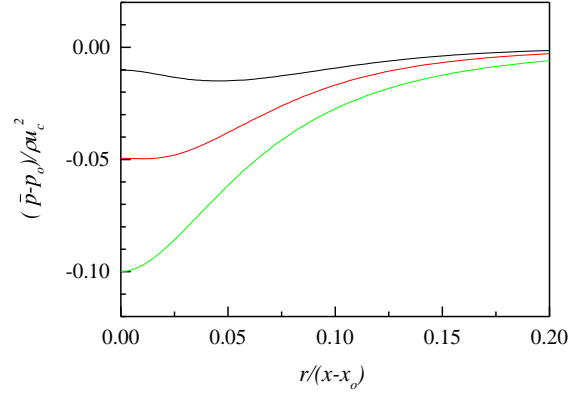


Figure 26. Mean static pressure profiles at $x/d: 10$ (—), 20 (—), 30 (—)

Solution of the normal stress $\overline{u'u'}$ is obtained from Eq. (18) along with the continuity equation for the scale factors $S = 0.03(x/d)^{-0.5}$ for the initial region, $S = 0.018(x/d)^{-0.5}$ for the intermediate region and $S = -0.06$ for the developed region considering NSE by equating the orders of magnitude of the proper terms. The normalized stress $\overline{u'u'}/u_c^2$ is plotted in Fig. 27 against r/d at $x/d=3, 10$ and 15 . Fellouah *et al.* [18] data of the normal stress provided for comparison are found in excellent agreement with those of the present simulation. Obtained solution with NSE at $x/d > 15$ proves to be able to predict the

axial evolution of the normal stress as observed in Fig. 28. While calculated normal stress without NSE, like the shear stress, are seen to increase rapidly in the downstream from $x/d=10-30$ (not shown). Fellouah *et al.* [18] and Hussein *et al.* [20] data included there for comparison are found in reasonable agreement with the present simulation.

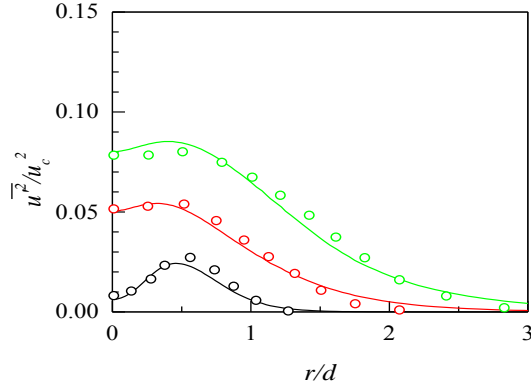


Figure 27. Axial normal stress profiles. Lines as in Fig. 25. Fellouah *et al.* data [18] (x/d : 3 (o), 10 (o), 15 (o))

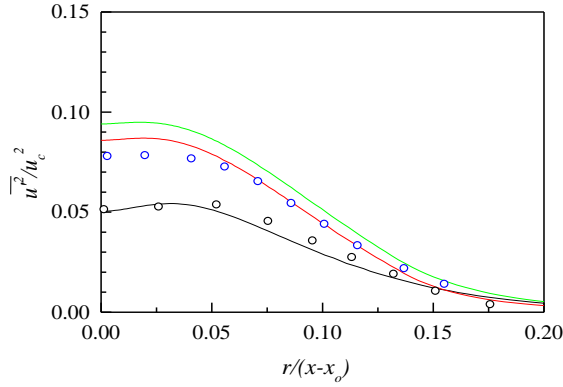


Figure 28. Axial normal stress profiles with NSE. Lines as in Fig. 26. Data of Fellouah *et al.* [18] (x/d : 10 (o)) and Hussein *et al.* [20] (o)

Solution of the normal stress $\overline{v'v'}$ is obtained by integrating Eq. (19) along with the continuity equation for $S = 0.4(x/d)^{0.5}$ in the initial region, $S=0.075$ in the intermediate region and $S=0.056$ in the developed region. The scale factors are determined by comparison of the magnitudes of the suitable terms of the equation where $\overline{v'v'}$ does not appear as axial derivative and does not require to consider NSE for the developed region. The stress $\overline{v'v'}/u_c^2$ is presented in Fig. 29 against r/d at $x/d=3, 10$ and 15 . Fellouah *et al.* [18] data of $\overline{v'v'}/u_c^2$ (taken here about twice of their v'/u_c being the values are somewhat less than the expected) added for comparison are found in excellent agreement with those of the present simulation. Figure 30

displays $\overline{v'v'}/u_c^2$ against $r/(x-x_0)$ at $x/d=10-30$. Fellouah *et al.* [18] and Hussein *et al.* [20] data included for comparison show fair agreement with that of the present simulation.

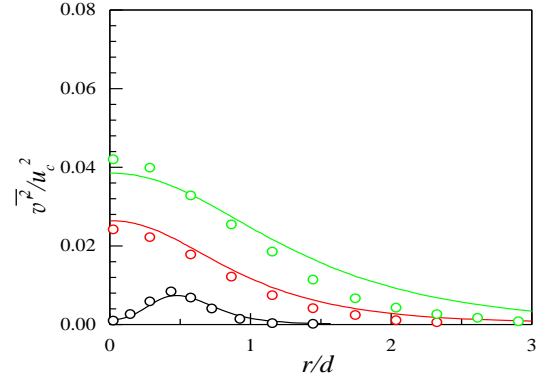


Figure 29. Radial normal stress profiles at x/d : 3 (—), 10 (—), 15 (—). Fellouah *et al.* [18] (x/d : 3 (o), 10 (o), 15 (o))

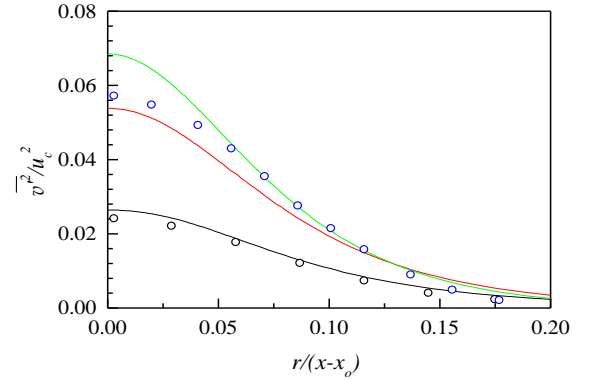


Figure 30. Radial normal stress profiles at x/d : 10 (—), 20 (—), 30 (—). Data of Fellouah *et al.* [18] (x/d : 10(o)) and Hussein *et al.* [20] (o)

Solution of the normal stress $\overline{w'w'}/u_c^2$ is obtained from Eq. (20) along with the continuity equation for $S=0.012$ at $x/d \leq 30$. The stress $\overline{w'w'}/u_c^2$ is depicted in Fig. 31 against r/d at $x/d=3, 10$ and 15 . The profiles of $\overline{w'w'}/u_c^2$ are displayed in Fig. 32 against $r/(x-x_0)$ at $x/d=10-30$ where Hussein *et al.* [20] data added for comparison are found in acceptable agreement.

5.2.3. Estimation of Scale Factor

In order to estimate the scale factor, nonlinear growth of the jet in the developing region ($x/d \leq 15$) is assumed as $\delta \sim x^{0.5}$ and linear growth in the self-similar region

($x/d > 15$) as $\delta \sim (x - x_0)$ in accordance with the literature [24, 31]. The assumption of linear growth of the jet at $x/d > 15$ is in excellent agreement with that of the present simulation. Experimental and computational data (e.g. [29, 32]) show that $\overline{u'u'}$ increases rapidly as linear in x at $x/d \leq 15$ and then decreases as x^{-1} at $x/d > 15$ indicating the axial variation of the fluctuating velocity scale u for the same regions. In determining S for Eq. (9), equating of the orders of magnitude of $\partial(\overline{u'v'})/\partial x$ and $\sqrt{\overline{v'^2}}\overline{v}$ for the viscosity dominated initial region ($x/d \leq 5$) yields $S = C_1$, and equating of $\partial(\overline{u'v'})/\partial x$ and $\overline{u}\partial\overline{v}/\partial x$ for $5 \leq x/d \leq 15$ yields $S = C_1 x^{1.5}$. Then comparison of the magnitudes of $\partial(\overline{u'v'})/\partial x$ and $\overline{u}\partial\overline{v}/\partial x$ along with NSE for $x/d > 15$ provides

$$C_1(1/xL) = -S(u_o^2/L)(\delta/L) \quad (31)$$

which on substitution of the scale functions becomes $S = -C_1/x$.

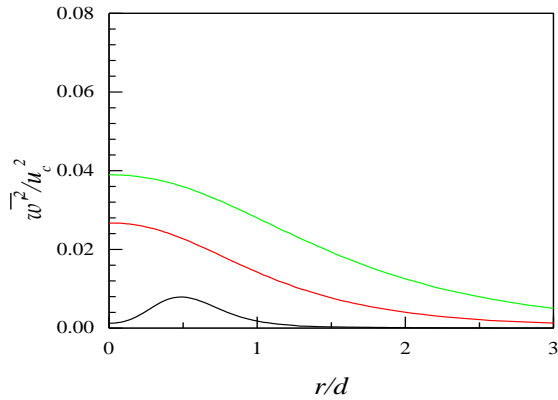


Figure 31. Azimuthal normal stress profiles. Lines as Fig. 29

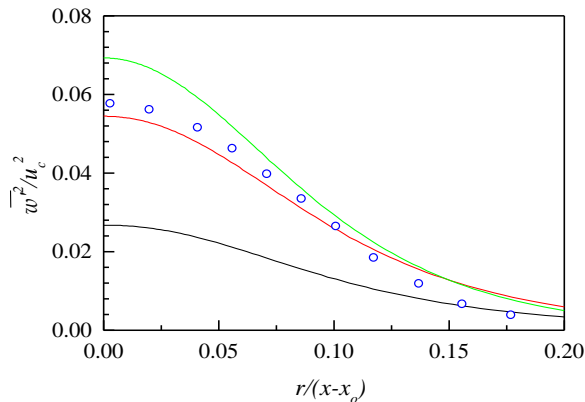


Figure 32. Azimuthal normal stress profiles. Lines as Fig. 30. Hussein *et al.* data [20] (o)

Scale factor is estimated for calculating \overline{p} , $\overline{u'u'}$, $\overline{v'v'}$ and $\overline{w'w'}$ from Eqs. (17)-(20), respectively, by the comparison of magnitudes of the appropriate terms. In estimating S for Eq. (17), comparison of the pressure and shear stress for $x/d \leq 15$ provides $S = C_2/x^{0.5}$ with two different values of C_2 for the initial and intermediate regions and equating of the pressure and inertia along with NSE provides $S = -C_2/x$ for $x/d > 15$. In evaluating S for Eq. (18), comparison of the normal stress and shear stress for $x/d \leq 15$ provides $S = C_3/x^{0.5}$ with two different values of C_3 for the initial and intermediate regions and equating of the normal stress and pressure for $x/d > 15$ along with NSE yields $S = -C_3$. Evaluation of S for Eq. (19) is made by simply equating the radial normal stress and shear stress as $S = C_4 x^{0.5}$ for the initial region and equating the normal stress and pressure yields $S = C_4$ with two different values of C_4 for the intermediate and developed regions. S is evaluated for Eq. (20) by equating the azimuthal and radial normal stresses as $S = C_5$ with a single value because axisymmetry requires that $\overline{v'v'} = \overline{w'w'}$ over the entire jet flow.

6. Further Discussion

Computational results show that $C_1 = 3.2$ for the additional Eq. (9) in the boundary layer flow implying that $\partial(\overline{u'v'})/\partial x$ and $\overline{u}\partial\overline{v}/\partial x$ are of equal orders of magnitude but $\partial(\overline{u'v'})/\partial x > \overline{u}\partial\overline{v}/\partial x$ while $C_1 = 1$ at $x/d > 15$ for the jet flow implying that $\partial(\overline{u'v'})/\partial x$ and $\overline{u}\partial\overline{v}/\partial x$ are of equal magnitudes. Moreover, $\sqrt{\overline{v'^2}}\overline{v}$ is seen larger than $\overline{u}\partial\overline{v}/\partial x$ in the initial region of the jet at the time of calculating the shear stress from Eq. (9). In most turbulent shear flows, Reynolds normal stresses bear the relation

$$\overline{u'u'} \approx 2\overline{v'v'} \approx 2\overline{w'w'}. \quad (32)$$

Using the turbulent structure parameter $-\overline{u'v'}/(\overline{u'u'} + \overline{v'v'} + \overline{w'w'}) \cong 0.15$ after Bradshaw *et al.* [33] and the shear correlation coefficient $-\overline{u'v'}/\sqrt{(\overline{u'u'}\overline{v'v'})} \cong 0.5$ after Klebanoff [14] along with Eqs. (8) and (32), the conditions $-\overline{u'v'}/\overline{u'u'} \approx 0.3$, $-\overline{u'v'}/\overline{v'v'} \approx 0.8$, $-\rho\overline{u'v'}/|\overline{p}| \approx 1$ can be derived for the boundary layer flow. In the free shear flow, the values of 0.135 and 0.4 for the turbulent structure parameter and the shear correlation coefficient after Pope [10] give the conditions $-\overline{u'v'}/\overline{u'u'} \approx 0.27$, $-\overline{u'v'}/\overline{v'v'} \approx 0.6$, $-\rho\overline{u'v'}/|\overline{p}| \approx 0.4$. Results from the present simulations at the last axial position of their calculation domains are seen to closely satisfy the above conditions across some fraction of the shear layer for both types of flow. It is to be noted for the boundary layer flow that in addition to the agreement with Klebanoff [14] data, the estimate of $\overline{w'w'}$ using Eq. (22) are

found in excellent agreement by DeGraaff and Eaton [30] with their experimental data.

7. Conclusions

Two-dimensional continuity and RANS equations for the mean motion occur with six unknowns for the boundary layer flow and with seven unknowns for the jet flow. In this study, one additional equation for the boundary layer flow while two additional equations for the jet flow are obtained from the transverse RANS equation using NMA and two other equations are obtained from the streamwise RANS equation using extended NMA to achieve the turbulence closure. The closed form equations are solved numerically that provide solutions for the mean streamwise velocity, mean transverse velocity, mean static pressure, and Reynolds shear stress and normal stresses. Results extracted from the simulation of both types of flow are found in overall agreement with the existing experimental data that proves the effectiveness of NMA in achieving the complete turbulence closure.

REFERENCES

- [1] I. Newton, "Methods of series and fluxions," The Mathematical Paper of Isaac Newton III (1670-1673), Cambridge Univ. Press, Cambridge, D.T. Whiteside ed. 50-71 (1969).
- [2] M. Kruskal, "Asymptotology in mathematical models in physical sciences," Proc. Conf. at Univ. of Notre Dame, S. Drobot ed., Prentice-Hall, New Jersey, 1963.
- [3] C.M. Bender and S.A. Orszag, Advanced Mathematical Methods for Scientists and Engineers (McGraw- Hill, New York, 1978).
- [4] T. Fishaleck and R.B. White, "The use of Kruskal-Newton diagrams for differential equations," Princeton Plasma Phys Lab-4289, New Jersey 1 (2008).
- [5] O. Reynolds, "On the dynamical theory of incompressible viscous fluids and determination of the criterion," Phil. Trans. Roy. Soc. A 186, 123 (1895).
- [6] P.A. Durbin and B.A.P. Reif, Statistical Theory and Modeling for Turbulent Flows (John Wiley and Sons, 2011).
- [7] L. Prandtl, "Über die ausgebildete turbulenz," ZAMM 5, 136 (1925).
- [8] W.P. Jones and B.E. Launder, "The prediction of laminarization with a two equation model," Int. J. Heat Mass Transfer 15, 301 (1972).
- [9] J. Boussinesq, "Theorie de l'ecoulement tourbillant," Mem. Pres. Acad. Sci. Inst. Fr. 23, 46 (1877).
- [10] S.B. Pope, Turbulent Flows (Cambridge University Press, Cambridge, 2000).
- [11] D.A. Anderson, J.C. Tannehill and R.H. Pletcher, Computational Fluid Mechanics and Heat Transfer (McGraw-Hill, New York, 1984).
- [12] L.H. Thomas, "Elliptic problems in linear difference equations over a network," Watson Sci. Comput. Lab. Report, Columbia University, New York, 1949.
- [13] A.A. Townsend, "The structure of the turbulent boundary layer," Proc. Cambridge Phil. Soc. 47, 375 (1951).
- [14] P.S. Klebanoff, "Characteristics of turbulence in boundary layer with zero pressure gradient," NACA TN-3178 (1954).
- [15] J. Muralis, H.M. Tsai and P. Bradshaw, "The structure of boundary layers at low Reynolds numbers," J. Fluid Mech. 122, 13 (1982).
- [16] D. Coles, "Measurements in the boundary layer on a smooth flat plate in supersonic flow, I. The problem of the turbulent boundary layer," Cal. Inst. Tech. JPL Report no. 20-69 (1953).
- [17] J. McQuaid, "Experiments on incompressible turbulent boundary layers with distributed injection," ARC Report no. 3549 (1967).
- [18] H. Fellouah, C.G. Ball and A. Pollard, "Reynolds number effects within the development region of a turbulent round free jet," Int. J. Heat and Mass Transfer 52, 3943 (2009).
- [19] H. Fellouah and A. Pollard, "The velocity spectra and turbulence length scale distributions in the near to intermediate regions of a round free turbulent jet," Phys. Fluids 21, 115101 (2009).
- [20] H.J. Hussein, S.P. Capp and W.K. George, "Velocity measurements in a high Reynolds number, momentum conserving axisymmetric turbulent jet," J. Fluid Mech. 258, 31 (1994).
- [21] H. Schlichting and K. Gersten, Boundary Layer Theory (Springer, Heidelberg, 2000).
- [22] M.A. Azim, "On the structure of a plane turbulent wall jet," ASME J. Fluids Eng. 135(8), 084502 (2013).
- [23] E. Ferdman, M.V. Otugen and S. Kim, "Effect of initial velocity profile on the development of the round jet," J. Propul. Power 16, 676 (2000).
- [24] G. Xu and R.A. Antonia, "Effect of different initial conditions on a turbulent round free jet," Exp. Fluids 33, 677 (2002).
- [25] B.J. Boersma, G. Brethouwer and F.T.M. Nieuwstadt, "A numerical investigation on the effect of inflow conditions on the self-similar region of a round jet," Phys. Fluids 10, 899 (1998).
- [26] H.E. Fielder, Control of free turbulent shear flows, Flow Control: Fundamentals and Practices (Springer-Verlag, Germany, 1998).
- [27] H. Tennekes and J.L. Lumley, A First Course in Turbulence (MIT Press, Massachusetts, 1972).
- [28] N.R. Panchapakesan and J.L. Lumley, "Turbulence measurements in axisymmetric jets of air and helium. Part 1: air jet," J. Fluid Mech. 246, 197 (1993).

- [29] W.R. Quinn, "Upstream nozzle shaping effects on near field flow in round turbulent free jets," *Euro J. Mechanics B/Fluids* 25, 279 (2006).
- [30] D.B. DeGraaff and J.K. Eaton, "Reynolds number scaling of the flat plate turbulent boundary layer," *J. Fluid Mech.* 422, 319 (2000).
- [31] L. Boguslawski and C.O. Popiel, "Flow structure of the free round turbulent jet in the initial region," *J. Fluid Mech.* 90, 531 (1979).
- [32] P.C. Babu and K. Mahesh, "Upstream entrainment in numerical simulations of spatially evolving round jets," *Phys. Fluids* 16(10), 3699 (2004).
- [33] P. Bradshaw, D.H. Ferriss and N.P. Atwell, "Calculation of boundary layer development using the turbulent energy equation," *J. Fluid Mech.* 28, 593 (1967).